Parity-protected anomalous diffraction in optical phase gradient metasurfaces

Yanyan Cao,[1] Yangyang Fu,[3,*] Lei Gao,[4] Huanyang Chen,[5] and Yadong Xu [1,2,†]

[1]*Institute of Theoretical and Applied Physics, School of Physical Science and Technology, Soochow University, Suzhou 215006, China*
[2]*Key Lab of Modern Optical Technologies of Education Ministry of China, Soochow University, Suzhou 215006, China*
[3]*College of Physics, Nanjing University of Aeronautics and Astronautics, and Key Laboratory of Aerospace Information Materials and Physics (NUAA), MIIT, Nanjing 211106, China*
[4]*Department of Photoelectric Science and Energy Engineering, Suzhou City University, Suzhou 215104, China*
[5]*School of Physics, Xiamen University, Xiamen 361005, China*

Optical phase gradient metasurfaces (PGMs) have provided unprecedented opportunities for arbitrarily controlling wave propagation via the generalized Snell's law (GSL). However, the whole picture of wave diffraction therein has not been clearly presented, particularly for the incident angles beyond the critical angle. Although a parity-dependent diffraction effect was found in acoustic metagratings, little is known about whether this effect holds true in typical optical PGMs. Here we demonstrate the universality of the parity-dependent diffraction effect by employing some optical PGMs with popular designs, such as all-dielectric and plasmonic meta-atoms. It is first shown that the parity in optical PGMs plays a significant role in determining the diffraction physics, producing a robust reversal effect of outgoing waves from the reflection to the transmission side. As an alternative degree of freedom in PGMs, the parity-dependent diffraction effect, together with the GSL, provides a complete theory to manipulate wave fields, further advancing various explorations in unique wave phenomena and promising applications.

I. INTRODUCTION

Optical phase gradient metasurfaces (PGMs) have attracted extensive attention in recent years owing to their powerful abilities on arbitrary control of light propagation [1–3], producing various significant effects, such as photonic spin Hall effect [4,5], ultrathin cloaking [6,7], retroreflection [8,9], anomalous refraction [10], and others [11–15]. The physical cornerstone behind these advances is the generalized Snell's law (GSL) [10] that is created by involving the phase gradient (ξ) along an optical interface, i.e., $k_0 \sin \theta_i = k_0 \sin \theta_{r(t)} - \xi$. However, this law is greatly challenged by full angle incidences, owing to the existence of the critical angle of GSL. When the incident angle is beyond the critical angle given as $\theta_c = \sin(1 - \xi/k_0)^{-1}$, the channel of lowest diffraction order is forbidden, and the incident wave cannot pass through the PGM via direct transmission. Essentially, optical PGMs are special diffraction gratings, which are structured arrays consisting of periodically arranged supercells with m unit cells (m is an integer). The m unit cells with different optical responses discretely introduce abrupt phase shifts covering the full range of 2π in a supercell, which can induce a phase gradient along the interface of two media. Many works [16–21] have reported theoretically and experimentally various diffraction phenomena in optical PGMs and the mentioned GSL was found to be the lowest diffraction order [see Fig. 1(a)]. Besides the anoma-

lous wave propagation via GSL, higher-order diffraction effects were also observed, while the underlying mechanism was not well solved, partially because ultrathin PGMs are too complex to be strictly analyzed. Although optical PGMs are very similar to conventional optical gratings (such as the blazed diffraction gratings), the complex diffraction properties of optical PGMs with special phase modulations cannot be fully understood by conventional diffraction equations.

Alternatively, by designing and studying an acoustic PGM model by introducing gradient index modulation into a subwavelength sound-hard material slit array, i.e., acoustic metagrating, a parity-dependent diffraction effect [22] was proposed to fully explain the higher-order diffraction effect. It was found that the integer m plays a fundamental role in determining the diffraction behavior of acoustic PGMs, leading to a set of equations for higher-order diffraction [22],

$$\begin{aligned} k_0 \sin \theta_i &= k_0 \sin \theta_t - nG, \ (L \text{ is odd}) \\ k_0 \sin \theta_i &= k_0 \sin \theta_r - nG, \ (L \text{ is even}) \end{aligned} \tag{1}$$

where θ_i and $\theta_{r(t)}$ represent the angle of the incident and reflected or transmitted light, $G = 2\pi/p$ is the reciprocal lattice vector, $p = ma$ is the period length of the supercell of the PGM, and a is the size of each unit cell in a supercell. The integer n indicates the diffraction order, and $L = m + n$ is the propagation number of multiple internal total reflections inside the PGM, i.e., the number of times that the waves travel inside the PGM. Usually, $G = |\xi|$, but they have different physical meanings [23]. A surprising finding in Eq. (1) is that the transmission and reflection through higher-order diffraction [$n \leqslant 0$ in Eq. (1)] can be completely reversed

---

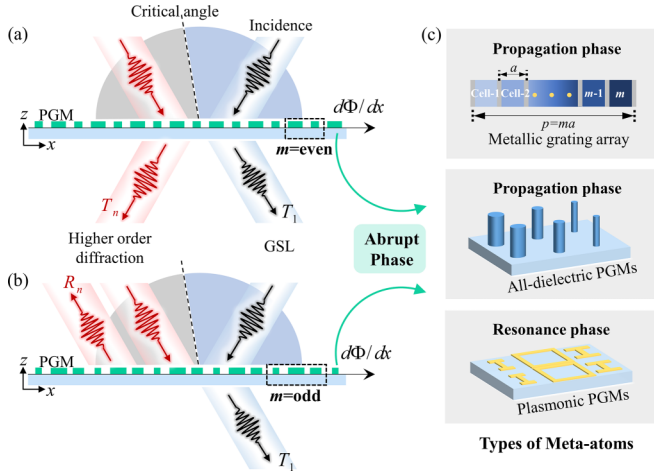*yyfu@nuaa.edu.cn
†ydxu@suda.edu.cn

FIG. 1. [(a),(b)] Sketch of the phase-gradient metasurfaces (PGMs) with m unit cells which are positioned at the interface between two ordinary media; the phase gradient is $\xi = d\Phi/dx$. For the incident angle below the critical angle (blue incident regions), the incident wave will couple to the transmitted wave (black arrows) of the lowest order [$n = 1$ in Eq. (1)], corresponding to GSL. For the incident angle beyond the critical angle (gray incident regions), the outgoing wave takes the higher-order diffraction [$n \leqslant 0$ in Eq. (1)], with the transmission or reflection (red arrows) depending on the number of unit cells m. (c) Schematic of the types of meta-atoms used to design optical PGMs: propagation phase and resonant phase.

by changing the parity design of integer m in the PGM [see Figs. 1(a) and 1(b)], and such phenomenon is very robust [22]. This parity-dependent diffraction effect provides an important principle to manipulate wave propagation in a versatile way beyond the limit of GSL [$n = 1$ in Eq. (1)], which has made important progress in acoustic and elastic metasurfaces [24–27], such as asymmetric vortex generation and propagation. However, as it is built on a specific model of PGMs, it seems that this parity-dependent diffraction effect is feasible only for acoustic waves and acoustic PGMs. No studies have been reported so far to show whether this effect holds true in the typical optical PGMs.

The aim of this work is to demonstrate the universality of this parity-dependent diffraction effect in optical PGMs with popular designs. This demonstration is necessary and fundamentally important, because the parity-dependent diffraction effect, which is complementary to the GSL, provides a complete theory for optical field manipulation using PGMs. A comprehensive understanding of high-order diffraction and its mechanism in optical PGMs is essential to realizing unique optical effects and promising applications. In the specific model [see the upper plot in Fig. 1(c)], two adjacent unit cells are separated by metal materials (they are equivalent to sound-hard materials in acoustics) to avoid near-field coupling across the interior boundary, and it ensures a steady phase gradient during the process of multiple internal total reflections in the PGM, which is even robust to the incident angle.

II. TYPICAL TYPE OF OPTICAL PGMs AND DISCUSSIONS

Referring to recent advances in optical PGMs [3], the major schemes to realize abrupt phase modulation can be divided

into two types [see Fig. 1(c)]. One type relies on the accumulated propagation phase of guided modes passing through the subwavelength dielectric cylinders and nanoscale pillars [28–30]; typical examples are all-dielectric metasurfaces at optical frequencies [see the middle plot in Fig. 1(c)]. The specific model used to reveal the parity-dependent diffraction effect is essentially of this type of propagation phase, except that there is no or very weak near-field coupling between guide modes in the specific model because the unit cells are separated by impenetrable metals. The other type is the resonant phase in the composite metal-dielectric structures, such as H-shaped antennas [5,31], and typical examples are plasmonic metasurfaces at microwave and terahertz frequencies. As we all know, in the acoustic PGM design, the neighbor couplings between adjacent unit cells are quite weak due to the presence of acoustic hard walls between them, which resemble some subwavelength waveguides, and the phase gradient is well preserved even for a larger incident angle. In optics, the impenetrable walls are not necessary to design optical PGMs and the neighbor coupling is relatively strong. The phase gradient enabled by the all-dielectric or plasmonic meta-atom design is not robust for a larger incident angle. In the following, we will demonstrate that the reversal phenomenon of transmission and reflection for higher diffraction order still exists in optical PGMs with popular designs, implying that the parity-dependent diffraction effect is universal even for optical PGMs with strong cross coupling. To be more convincing, we consider these typical nanostructures from previous reports in the literature [29,31] to design these optical PGMs, in which the geometric and material parameters are consistent with the experiments.

III. DEMONSTRATION OF THE ALL-DIELECTRIC PGMs

First, we design the all-dielectric PGMs, an infinite array of dielectric nanoblocks (refractive index $n_1 = 5$) on top of a semi-infinite fused silica substrate (refractive index $n_2 = 1.45$). The lattice constant of the nanoblock (unit cell) is $a_1 = 420$ nm and its height is $h = 500$ nm [see the inset of Fig. 2(a)]. The incident light propagating along the z axis is a plane wave, with the electric and magnetic fields polarized along the y and x axes, respectively. The working wavelength is $\lambda_0 = 1550$ nm. COMSOL MULTIPHYSICS is employed to perform numerical simulations. Figures 2(a) and 2(b) show the numerically calculated results of the transmittance and the corresponding phase as a function of the length (d_x) and width (d_y) of the nanoblock. To ensure the good performance of an all-dielectric PGM, the transmission efficiencies of the designed cells are around 90% and the phase difference of two adjacent cells is nearly $2\pi/m$, as required by the design of a PGM. Due to the lattice constant $a_1 = 420$ nm, the length and width of the nanoblock are less than 380 nm. By arranging the discrete phase meta-atoms sequentially in the x direction to form a supercell, we can obtain the desired all-dielectric PGMs by periodically replicating this supercell in both the x and y directions. We design two all-dielectric PGMs with $m = 2$ and 3 to reveal the scattering reversal effect of higher-order diffraction, which can demonstrate the parity-dependent diffraction effect. For the $m = 2$ case, the geometric parameters of the two nanoblocks are marked by
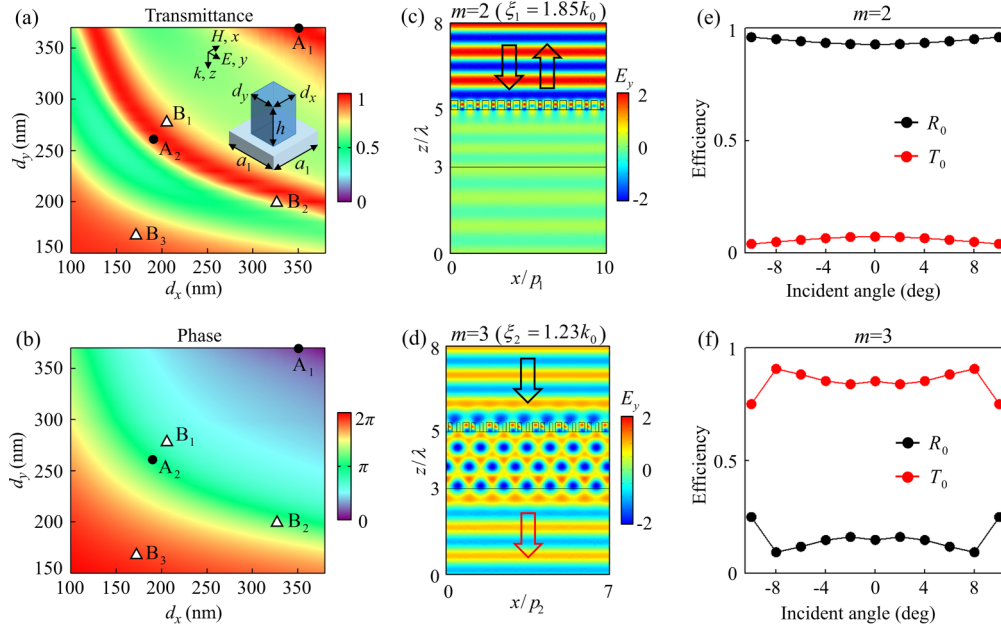
FIG. 2. The parity-dependent phenomena in all-dielectric PGMs. (a) Transmittance variation for the meta-atom and (b) the transmitted phase as a function of nanoblock size d_x and d_y. Inset is schematic of a high refractive index dielectric nanoblock meta-atom on top of a bulk-fused silica substrate. The height of the nanoblock is $h = 500$ nm and the lattice constant is $a_1 = 420$ nm. In the plots, A_1 and A_2 represent the corresponding sizes of two unit cells in the PGM with $m = 2$; B_1, B_2, and B_3 represent the corresponding sizes of three unit cells in the PGM with $m = 3$. [(c),(d)] are the simulated total electric field patterns of two PGMs with $m = 2$ ($\xi_1 = 1.85k_0$) and $m = 3$ ($\xi_2 = 1.23k_0$) at the normal incidence. [(e),(f)] are the relationships between the transmission and reflection efficiency of the higher diffraction order ($n = 0$) and the incident angle in the two designed PGMs.

A_1 ($d_x = 350$ nm and $d_y = 370$ nm) and A_2 ($d_x = 190$ nm and $d_y = 260$ nm) and their corresponding phase and transmission are ($\phi = 0$, $T = 0.99$) at A_1 and ($\phi = \pi$, $T = 0.90$) at A_2, respectively, as seen in Figs. 2(a) and 2(b). For the case of $m = 3$, the corresponding geometry sizes are indicated by B_1 ($d_x = 204$ nm and $d_y = 280$ nm), B_2 ($d_x = 324$ nm and $d_y = 200$ nm), and B_3 ($d_x = 170$ nm and $d_y = 170$ nm). The corresponding transmission phase and transmittance are ($\phi = 0.58\pi$, $T = 0.86$) at B_1, ($\phi = 1.22\pi$, $T = 0.79$) at B_2, and ($\phi = 1.89\pi$, $T = 0.88$) at B_3, respectively.

Given that the lattice constant of each meta-atom is $a_1 = 420$ nm, thus the length of a supercell is $p_1 = 840$ nm for $m = 2$, and $p_2 = 1260$ nm for $m = 3$. In this case, the phase gradients of the two PGMs are $\xi_1 = 2\pi/p_1 = 1.85k_0$ and $\xi_2 = 2\pi/p_2 = 1.23k_0$, and the direction of the phase gradient is along the $+x$ direction. According to the GSL, these designed PGMs have critical angles, which are $\theta_c = \arcsin(1 - \xi_1/k_0) = -57.7°$ and $\theta_c = \arcsin(1 - \xi_2/k_0) = -13.3°$, respectively. When the incident angle is beyond the critical angle $\theta_{\rm in} > \theta_c$, the GSL fails to predict the outgoing waves and the outgoing waves will obey the parity-dependent diffraction effect [Eq. (1)] [22]. For example, when the incident angle is $\theta_{\rm in} = 0°$, which is beyond the critical angle in both cases, the outgoing wave can take the higher-order diffraction of $n = 0$ and the corresponding propagation number in PGM with m unit cells is $L = m + 0 = m$. According to Eq. (1), when m is even, e.g., $m = 2$, the propagation number L is even, which leads to the reflection of the $n = 0$ order and the reflection angle is $\theta_r = 0°$. When m is odd, e.g., $m = 3$, the propagation number L is odd, which results in the transmission of the $n = 0$ order and the transmission angle is $\theta_t = 0°$. This

scattering reversal effect of the higher-order diffraction is confirmed by these two designed all-dielectric PGMs. We show the simulated electric field patterns of the designed PGMs with $m = 2$ and $m = 3$ in Figs. 2(c) and 2(d), respectively. It is clearly seen that for normal incidence ($\theta_{\rm in} = 0°$), nearly total reflection happens in the PGM with $m = 2$ [see the black arrow in Fig. 2(c)] and nearly total transmission occurs in the PGM with $m = 3$ [see the red arrow in Fig. 2(d)]. Not limited to the normal incidence, a similar reversal effect happens for other incident angles at which the outgoing waves take the higher diffraction order. To quantify such angular performance, we numerically calculated the relationship between the transmission or reflection of the higher diffraction order ($n = 0$) and the incident angle. For the $m = 2$ case [see Fig. 2(e)], more than 93% reflection efficiency of the $n = 0$ order is observed for $\theta_{\rm in} \in [-10°, 10]$. However, for the $m = 3$ case [see Fig. 2(f)], the reflection is reversed to transmission due to the integer-parity transition of the cell number, and the transmission efficiency of the $n = 0$ order reaches 85% for $\theta_{\rm in} = 0°$, which is quite high considering the unavoidable reflections due to impedance mismatches. Therefore, the parity-dependent diffraction effect is well demonstrated in the all-dielectric PGMs.

IV. DEMONSTRATION OF THE PLASMONIC PGMs

We further check the parity-dependent diffraction effect by designing two plasmonic PGMs with odd and even unit cells; the designed unit cells are based on the sandwich structures made of metal and dielectric materials [31]. As shown in Fig. 3, the unit cells are composed of three layers of metallic
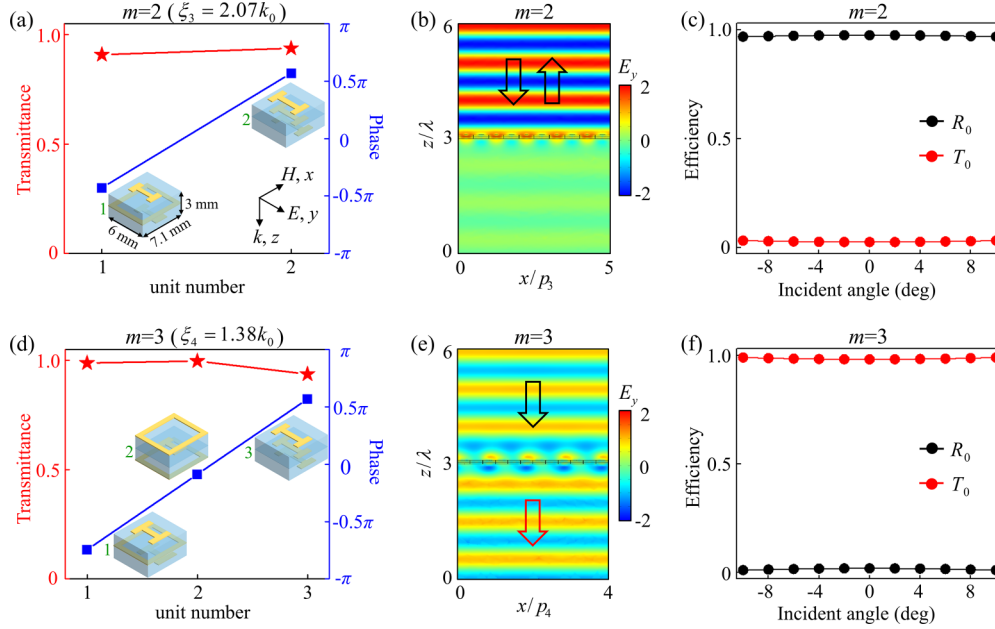
FIG. 3. The parity-dependent phenomena in the plasmonic PGMs. [(a),(d)] Numerically calculated transmission amplitude and phase of the unit cells for the plasmonic PGMs with $m = 2$ and $m = 3$. In both cases, the phase change between every two adjacent unit cells satisfies $2\pi/m$. Insets are 3D illustrations of the designed unit cells for the plasmonic PGMs; the yellow parts are metallic patterns and the blue regions are dielectric spacers. The geometric parameters are obtained from Ref. [31]. [(b),(e)] are simulated total electric field patterns of the two designed PGMs with $m = 2$ ($\xi_3 = 2.07k_0$) and $m = 3$ ($\xi_4 = 1.38k_0$) at the normal incidence. [(c),(f)] are the relationships between transmission and reflection efficiency of the higher diffraction order ($n = 0$) and the incident angle in the two designed PGMs.

patterns separated by a thin dielectric spacer. The length, width, and thickness of the unit cells are 7.1, 6.0, and 3.0 mm, respectively, referring to Ref. [31]. By changing the geometry sizes of the sandwich structures, their transmission and phase profiles could be obtained from numerical simulations and the working frequency is considered at 10.2 GHz. Here we directly give out the final results of the transmission and phase of these cells in the two plasmonic PGMs with $m = 2$ and $m = 3$. For the case of $m = 2$, the phase and transmission of the two cells are ($\phi = -0.43\pi$, $T = 0.84$) and ($\phi = 0.57\pi$, $T = 0.88$), respectively [see Fig. 3(a)]. For the case of $m = 3$, they are ($\phi = -0.75\pi$, $T = 0.98$), ($\phi = -0.09\pi$, $T = 0.99$), and ($\phi = 0.57\pi$, $T = 0.88$), respectively [see Fig. 3(d)]. By contiguously arranging the two (three) unit cells, we obtain the plasmonic PGM with $m = 2$ ($m = 3$). The lengths of the supercell are $p_3 = 14.2$ mm for $m = 2$ and $p_4 = 21.3$ mm for $m = 3$, with the phase gradient calculated as $\xi_3 = 2\pi/p_3 = 2.07k_0$ and $\xi_4 = 2\pi/p_4 = 1.38k_0$. The corresponding critical angle is $\theta_c = \arcsin(1 - \xi_4/k_0) = -22.5°$ for the case of $m = 3$, while for $m = 2$, due to the phase gradient $\xi_3 > 2k_0$, only the $n = 0$ diffraction order exists for the outgoing waves. In other words, the incident wave is totally reflected among the whole incident range [2]. Figure 3(b) shows the simulated field patterns when a plane wave is normally incident on the plasmonic PGM with $m = 2$, where nearly perfect reflection is seen. However, for the PGM with $m = 3$, as shown in Fig. 3(e), the normally incident wave can pass through the plasmonic PGM with high transmittivity. Moreover, Figs. 3(c) and 3(f) show the corresponding relationship between the transmission and reflection of the higher diffraction order ($n = 0$) and the incident angle. For the case of $m = 2$ [see Fig. 3(c)], more than 97% reflection efficiency

of the $n = 0$ order is observed for $\theta_{\mathrm{in}} \in [-10°, 10°]$. For the case of $m = 3$ [see Fig. 3(f)], the transmission efficiency of the $n = 0$ order is more than 98% with $\theta_{\mathrm{in}} \in [-10°, 10°]$. These results confirm the parity-dependent diffraction effect again.

We further study all the diffraction behaviors using the designed plasmonic PGMs with $m = 2$ and $m = 3$, which can demonstrate the rules of the GSL and the parity-dependent diffraction effect. Figure 4(a) shows the corresponding results for the plasmonic PGM with $m = 2$. As the phase gradient is $\xi_3 > 2k_0$, only the higher-order diffraction of $n = 0$ can exist in the whole incident range $\theta_{\mathrm{in}} \in [-80°, 80°]$, which leads to the high-efficiency reflection (more than 91%) due to an even propagation number of $L = 2$. For illustrations, Fig. 4(b) shows the simulated electric field patterns for $\theta_{\mathrm{in}} = -45°$ and $\theta_{\mathrm{in}} = 45°$, where the high reflection of the $n = 0$ order is seen in both cases. For the PGM with $m = 3$, as shown in Fig. 4(c), the critical angle is $\theta_c = -22.5°$. When $\theta_{\mathrm{in}} < -22.5°$, the propagation number is $L = 1$; then it is mainly the transmitted wave of the $n = 1$ order following the GSL [see the green curve in Fig. 4(c)]. For example, when the incident angle is $\theta_{\mathrm{in}} = -45°$, the anomalous transmission efficiency is 67%. However, the GSL is insufficient to predict the anomalous diffraction waves for the incident angle beyond the critical angle ($\theta_{\mathrm{in}} > -22.5°$). Following the parity-dependent diffraction principle, it is the transmitted wave of the $n = 0$ order for $22.5° > \theta_{\mathrm{in}} > -22.5°$ owing to the odd propagation number of $L = m + n = 3$, while it is the reflected wave of the $n = -1$ order for $\theta_{\mathrm{in}} > 22.5°$ owing to the even propagation number of $L = m + n = 2$. The diffraction efficiency of the $n = 0$ order is higher than these of $n = 1$ and $n = -1$, because the phase gradient is better maintained for a smaller incident angle. In particular, the efficiency of the transmitted wave
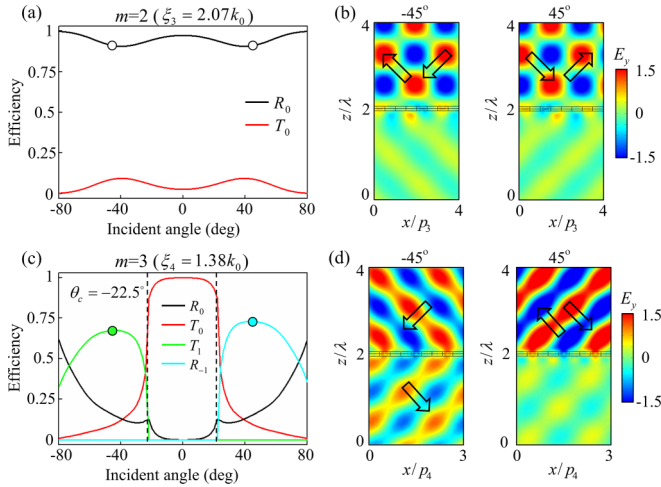
FIG. 4. [(a),(c)] are the relationships between transmission and reflection of all diffraction orders and the incident angle in the plasmonic PGMs with $m = 2$ and $m = 3$. (b,d) are simulated total electric field patterns of the plasmonic PGMs with $m = 2$ and $m = 3$, respectively, at $\theta_{in} = -45°$ and $\theta_{in} = 45°$. The arrows in the plots represent the propagation directions of incident and reflected or transmitted waves.

following the GSL at $\theta_{in} = -45°$ is almost equal to that of the reflected wave at $\theta_{in} = 45°$ that takes the parity-dependent effect. The simulated electric field patterns of the plasmonic PGMs with $m = 3$ are displayed in Fig. 4(d) for the incidences of $\theta_{in} = -45°$ and $\theta_{in} = 45°$. When the incident angle is $\theta_{in} = -45°$, the incident waves following the GSL can pass through the PGM and the transmission angle is $\theta_t = 42°$. When the incident wave is $\theta_{in} = 45°$, the incident wave taking the higher-order diffraction of $n = -1$ is reflected by the PGM and the reflection angle is $\theta_r = -42°$. All these results indicate that the parity-dependent diffraction effect is universal, even for the optical PGMs with strong cross coupling.

V. MULTIPLE RESONANCES IN OPTICAL PGMs

In the previous work, the parity-dependent diffraction principle was proposed by employing the PGMs with isolated meta-atoms [22]. Due to the presence of impenetrable walls between adjacent unit cells, which resemble some subwavelength waveguides, only the fundamental mode can be supported inside these unit cells. Therefore, one may doubt that this parity-dependent diffraction principle cannot be applicable to optical PGMs with nonisolated meta-atoms. In order to reveal the physical mechanism of the parity-dependent diffraction effect in optical PGMs based on the resonance phase, transient simulations were carried out by using COMSOL MULTIPHYSICS. Here we discuss the case of ultrathin plasmonic PGMs with $m = 3$ as shown in Fig. 3. Due to $\xi_4 = 1.38k_0$, when the incident angle is $\theta_{in} = 0°$, the effective higher diffraction order is $n = 0$. The multiple resonances will occur inside the plasmonic PGMs and the corresponding resonance number is $L = m + n = 3$. The odd L leads to the transmission of the $n = 0$ order. This property is consistent with the PGMs of the propagation phase reported previously [22]. In addition, we design a subwavelength uniform plasmonic metasurface for comparison, with the period including only one unit cell ($m = 1$), i.e., the unit cell 1 in Fig. 3(d). Since there is no phase gradient and the period length (7.1 mm) is much smaller than the incident wavelength, when the incident angle is $\theta_{in} = 0°$, the incident wave will couple to the transmitted wave of the lowest order, $n = 1$, and the resonance number is $L = 1$, which is independent of m.

In simulations, we chose the continuous plane wave to excite the plasmonic PGMs ($m = 3$) and the subwavelength uniform plasmonic metasurface ($m = 1$), respectively, and obtained simulated results at different time instants as shown in Fig. 5. In the plots, the black arrows indicate the propagation directions of the incident and transmitted waves. At 200 ps, the two continuous plane waves are generated synchronously with the incident angle of $\theta_{in} = 0°$ on the plasmonic PGMs and the uniform metasurface, respectively, and reach their
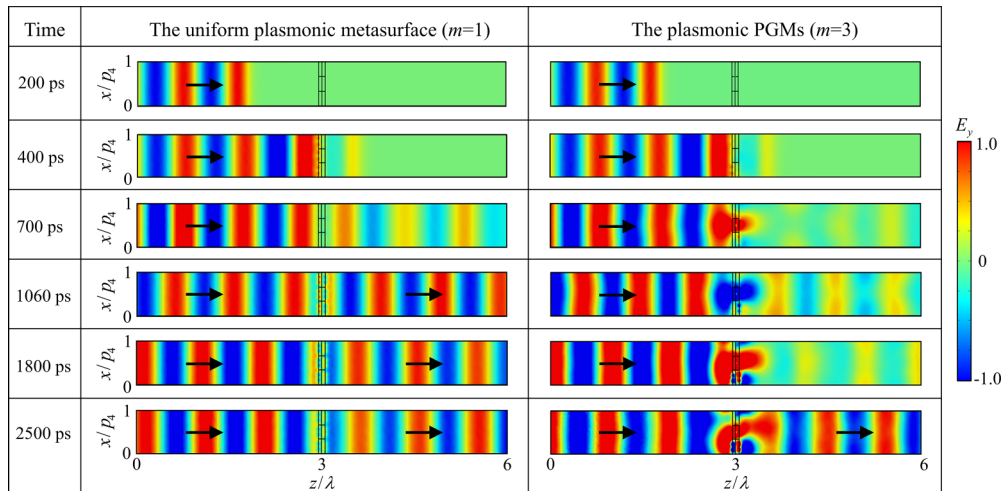

FIG. 5. Transient simulations for the plasmonic PGMs with $m = 3$ and the subwavelength uniform plasmonic metasurface with $m = 1$. The black arrows represent the propagation directions of the incident and transmitted waves, and the working frequency is considered at 10.2 GHz. The time when a snapshot of the fields is taken is marked on the left side of the field patterns. It indicates that the multiple resonance process occurs within the plasmonic PGMs.

surface at 400 ps. For the uniform metasurface, at 1060 ps, the amplitude of the transmitted electric field is close to 1 and it has a perfect wavefront, indicating that the incident wave is completely transmitted. However, for the plasmonic PGMs, at 1060 and 1800 ps, the incident waves are still localized inside the plasmonic PGMs, and the transmitted electric fields are very weak. At 2500 ps, the amplitude of the transmitted electric field is close to 1 and the wavefront is perfect, almost consistent with the steady simulated field pattern shown in Fig. 3(e). This implies that the incident wave completely passes through the plasmonic PGMs at this time. Obviously, complete transmission in the plasmonic PGMs takes much more time, almost three times as long as to the uniform metasurface. This is consistent with the above analysis, as the multiple resonances take place inside the plasmonic PGMs in the higher-order diffraction, and the number of resonance times L is related to the number of unit cells m. Therefore, we have revealed the physical mechanism of the higher-order diffraction in the optical PGMs from the perspective of multiple resonances.

VI. CONCLUSION

In conclusion, by designing several optical PGMs consisting of all-dielectric and plasmonic meta-atoms, we have demonstrated the universality of the parity-dependent diffrac- tion effect in optical PGMs with strong neighbor coupling. It is found that the parity design in these PGMs plays a pivotal role in the higher-order diffraction for incident angles beyond the critical angle. Specifically, the transmission and reflection through the higher-order diffraction are completely reversed by changing the parity design of the meta-atom number in the designed PGMs, which is the key feature of the parity- dependent diffraction effect. These results further confirm the parity-dependent diffraction effect theoretically proposed and experimentally demonstrated in acoustics; it is also universal even for the optical PGMs. Considering recent advances in acoustics [26], we believe that the parity-dependent effect can provide an alternative way to manipulate light fields, enabling some new optical phenomena and potential applications.

[1] N. Yu and F. Capasso, Flat optics with designer metasurfaces, Nat. Mater. **13**, 139 (2014).

[2] Y. Xu, Y. Fu, and H. Chen, Planar gradient metamaterials, Nat. Rev. Mater. **1**, 16067 (2016).

[3] S. Sun, Q. He, J. Hao, S. Xiao, and L. Zhou, Electromagnetic metasurfaces: Physics and applications, Adv. Opt. Photonics **11**, 380 (2019).

[4] X. Yin, Z. Ye, J. Rho, Y. Wang, and X. Zhang, Photonic spin Hall effect at metasurfaces, Science **339**, 1405 (2013).

[5] W. Luo, S. Xiao, Q. He, S. Sun, and L. Zhou, Photonic spin Hall effect with nearly 100% efficiency, Adv. Opt. Mater. **3**, 1102 (2015).

[6] X. Ni, Z. J. Wong, M. Mrejen, Y. Wang, and X. Zhang, An ultrathin invisibility skin cloak for visible light, Science **349**, 1310 (2015).

[7] Y. Yang, L. Jing, B. Zheng, R. Hao, W. Yin, E. Li, C. M. Soukoulis, and H. Chen, Full-polarization 3D metasurface cloak with preserved amplitude and phase, Adv. Mater. **28**, 6866 (2016).

[8] A. Arbabi, E. Arbabi, Y. Horie, S. M. Kamali, and A. Faraon, Planar metasurface retroreflector, Nat. Photonics **11**, 415 (2017).

[9] Y. Fu, Y. Cao, and Y. Xu, Multifunctional reflection in acoustic metagratings with simplified design, Appl. Phys. Lett. **114**, 053502 (2019).

[10] N. Yu, P. Genevet, M. A. Kats, F. Aieta, J.-P. Tetienne, F. Capasso, and Z. Gaburro, Light propagation with phase discon- tinuities: Generalized laws of reflection and refraction, Science **334**, 333 (2011).

[11] S. Wang, P. C. Wu, V.-C. Su, Y.-C. Lai, C. H. Chu, J.-W. Chen, S.-H. Lu, J. Chen, B. Xu, C.-H. Kuan, T. Li, S. Zhu, and D. P. Tsai, Broadband achromatic optical metasurface devices, Nat. Commun. **8**, 187 (2017).

[12] D. Lin, P. Fan, E. Hasman, and M. L. Brongersma, Dielectric gradient metasurface optical elements, Science **345**, 298 (2014).

[13] X. Wan, X. Shen, Y. Luo, and T. J. Cui, Planar bifunctional Luneburg-fisheye lens made of an anisotropic metasurface, Laser Photonics Rev. **8**, 757 (2014).

[14] M. Khorasaninejad, W. T. Chen, R. C. Devlin, J. Oh, A. Y. Zhu, and F. Capasso, Metalenses at visible wavelength: Diffraction-limited focusing and subwavelength resolution imaging, Science **352**, 1190 (2016).

[15] W. Luo, S. Sun, H.-X. Xu, Q. He, and L. Zhou, Transmissive Ultrathin Pancharatnam-Berry Metasurfaces with Nearly 100% Efficiency, Phys. Rev. Appl. **7**, 044033 (2017).

[16] S. Larouche and D. Smith, Reconciliation of generalized refrac- tion with diffraction theory, Opt. Lett. **37**, 2391 (2012).

[17] Y. Xu, Y. Fu, and H. Chen, Steering light by a subwavelength metallic grating from transformation optics, Sci. Rep. **5**, 12219 (2015).

[18] N. Estakhri and A. Alù, Wave-Front Transformation with Gra- dient Metasurfaces, Phys. Rev. X **6**, 041008 (2016).

[19] A. Epstein and G. Eleftheriades, Synthesis of Passive Lossless Metasurfaces Using Auxiliary Fields for Reflectionless Beam Splitting and Perfect Reflection, Phys. Rev. Lett. **117**, 256103 (2016).

[20] Y. Ra'di, D. Sounas, and A. Alù, Metagratings: Beyond the Limits of Graded Metasurfaces for Wave Front Control, Phys. Rev. Lett. **119**, 067404 (2017).

[21] A. Wong and G. Eleftheriades, Perfect Anomalous Reflection with a Bipartite Huygens' Metasurface, Phys. Rev. X **8**, 011036 (2018).

[22] Y. Fu, C. Shen, Y. Cao, L. Gao, H. Chen, C. T. Chan, S. A. Cummer, and Y. Xu, Reversal of transmission and reflection based on acoustic metagratings with integer parity design, Nat. Commun. **10**, 2326 (2019).

[23] Y. Cao, Y. Fu, Q. Zhou, X. Ou, L. Gao, H. Chen, and Y. Xu, Mechanism behind Angularly Asymmetric Diffraction in Phase-Gradient Metasurfaces, Phys. Rev. Appl. **12**, 024006 (2019).

[24] B. Li, Y. Hu, J. Chen, G. Su, Y. Liu, M. Zhao, and Z. Li, Efficient Asymmetric Transmission of Elastic Waves in Thin Plates with Lossless Metasurfaces, Phys. Rev. Appl. **14**, 054029 (2020).

[25] Y. Hu, Y. Zhang, G. Su, M. Zhao, B. Li, Y. Liu, and Z. Li, Realization of ultrathin waveguides by elastic metagratings, Commun. Phys. **5**, 62 (2022).

[26] Y. Fu, Y. Tian, X. Li, S. Yang, Y. Liu, Y. Xu, and M. Lu, Asymmetric Generation of Acoustic Vortex Using Dual-Layer Metasurfaces, Phys. Rev. Lett. **128**, 104501 (2022).

[27] Y. Fu, C. Shen, X. Zhu, J. Li, Y. Liu, S. A. Cummer, and Y. Xu, Sound vortex diffraction via topological charge in phase gradient metagratings, Sci. Adv. **6**, eaba9876 (2020).

[28] S. Chen, Z. Li, Y. Zhang, H. Cheng, and J. Tian, Phase manipulation of electromagnetic waves with metasurfaces and its applications in nanophotonics, Adv. Opt. Mater. **6**, 1800104 (2018).

[29] M. I. Shalaev, J. Sun, A. Tsukernik, A. Pandey, K. Nikolskiy, and N. M. Litchinitser, High-efficiency all-dielectric metasurfaces for ultracompact beam manipulation in transmission mode, Nano Lett. **15**, 6261 (2015).

[30] M. Khorasaninejad, A. Y. Zhu, C. Roques-Carmes, W. T. Chen, J. Oh, I. Mishra, R. C. Devlin, and F. Capasso, Polarization-insensitive metalenses at visible wavelengths, Nano Lett. **16**, 7229 (2016).

[31] H. Chu, Q. Li, B. Liu, J. Luo, S. Sun, Z. H. Hang, L. Zhou, and Y. Lai, A hybrid invisibility cloak based on integration of transparent metasurfaces and zero-index materials, Light: Sci. Appl. **7**, 50 (2018).